nature photonics

ARTICLES

PUBLISHED ONLINE: 23 FEBRUARY 2014 | DOI: 10.1038/NPHOTON.2014.2

Electrically driven subwavelength optical nanocircuits

Kevin C. Y. Huang[1,2†], Min-Kyo Seo[1,3†*], Tomas Sarmiento[2], Yijie Huo[2], James S. Harris[2] and Mark L. Brongersma[1*]

The miniaturization of electronic and photonic device technologies has facilitated information processing and transport at ever-increasing speeds and decreasing power levels. Nanometallics or 'plasmonics' has empowered us to break the diffraction limit and open the door to the development of truly nanoscale optical circuits. A logical next step in this development is the realization of compact optical sources capable of electrically driving such nanocircuits. Nanometallic lasers are a possible candidate, but the realization of power-efficient, electrically pumped nanolasers at room temperature is extremely challenging. Here, we explore a plasmonic light-emitting diode as a possible alternative option. We demonstrate that an electrically driven, nano light-emitting diode is capable of directing light emission into a single-mode plasmon waveguide with a cross-sectional area of $0.016\lambda^2$ by exploiting the Purcell effect. With this source, electrically driven subwavelength optical nanocircuits for routing, splitting, free-space coupling and directional coupling are realized for the first time.

In recent years, significant advancements have been made in realizing nanoscale circuits capable of manipulating light below the diffraction limit[1]. Such circuits can find application in optical communication[2], quantum plasmonics[3] and nanoscale biosensing elements[4]. One of the important next steps in this development is the realization of optical sources capable of electrically driving such circuits. Nanolasers may provide a viable option as they afford single-mode emission and the generation of coherent radiation within an extremely small footprint[5,6]. However, despite many demonstrations of nanolasers based on metallic[7–12], metallo–dielectric[13,14] and dielectric[15–18] nanocavities, the fundamental trade-off between cavity size and cavity loss, as well as the challenges with electrical injection, continues to pose a significant challenge in the realization of power-efficient and electrically pumped subwavelength-scale lasers that can operate at room temperature[19,20]. Moreover, on-chip optical interconnect applications, mobile devices and on-body sensing systems set particularly stringent power consumption requirements on sources where the achievement of a low lasing threshold is necessary but may not be sufficient.

In this Article, we address the traditional trade-offs in nanolaser cavity design by developing an electrically driven metal-clad nanoscale light-emitting diode (nano-LED) with a subwavelength device footprint capable of directing some of its emission into a single-mode waveguide, as shown in Fig. 1. This slot-waveguide-coupled nano-LED is conceptually related to several recent demonstrations of surface plasmon-emitting diodes (SPEDs)[21–24] that generate propagating one-dimensionally confined surface plasmons or metal–dielectric–metal (MDM) gap plasmons by placing a light-emitting material inside or close to two semi-infinite planar metal slabs. Although one-dimensionally confined gap plasmons demonstrate relatively low loss, low leakage and efficient coupling to a silicon slab waveguide[25], they do not offer the lateral field confinement that is essential in practical interconnects. In this work we demonstrate the electrical generation of subwavelength two-dimensionally confined gap plasmon modes. Such two-dimensionally confined modes are suitable for chip-scale applications that require flexible routing of optical signals and dense integration of complex nanophotonic circuit elements[26,27].

Our proposed source, which incorporates an emitting semiconductor quantum well in an ultracompact metal slot waveguide[28–33], has several desirable properties. First, a modification of the local density of optical states inside the slot waveguide helps to direct the emission into the gap plasmon mode[31–33], while ohmic losses in the metal via lossy wave excitation are suppressed[34]. Second, spontaneous emission enhancement increases the radiative decay rate of the active semiconductor medium[35], allowing high-speed modulation of the nano-LED[36] without using non-radiative carrier quenching methods[37–41]. Third, the guided emission rapidly transitions out of the lossy metal-clad active emission region into a metal–air–metal slot waveguide with much lower propagation loss, facilitating high power efficiency. Finally, the metal in this source offers simultaneous current injection, optical guiding and thermal dissipation functions in a compact subwavelength physical space. This type of multifunctionality allows for denser integration with electrically compatible devices. Although the emission from nano-LEDs is broadband and incoherent, they may serve as an efficient and high-speed alternative light source[37–42] to nanolasers in a variety of applications.

Slot-waveguide-coupled nano-LED platform

At the heart of our electrically driven subwavelength plasmonic nanocircuits is a 130-nm-tall and 60-nm-wide ridge LED containing a single InGaAs/GaAs quantum well emitting at a free-space wavelength of $\lambda_0 = 970$ nm. Electrical injection occurs through an equally wide self-aligned p-contact on the quantum-well ridge and the substrate that serves as the n-contact. An 80-nm-wide slot is milled in the gold slab starting from the output facet of the

[1]Geballe Laboratory for Advanced Materials, Stanford University, McCullough Building, 476 Lomita Mall, Stanford, California 94305-4045, USA, [2]Department of Electrical Engineering, Stanford University, David Packard Building, 350 Serra Mall, Stanford, California 94305-9505, USA, [3]Department of Physics and Institute for the NanoCentury, KAIST, Daejeon 305-701, South Korea; †These authors contributed equally to this work. *e-mail: minkyo_seo@kaist.ac.kr; brongersma@stanford.edu

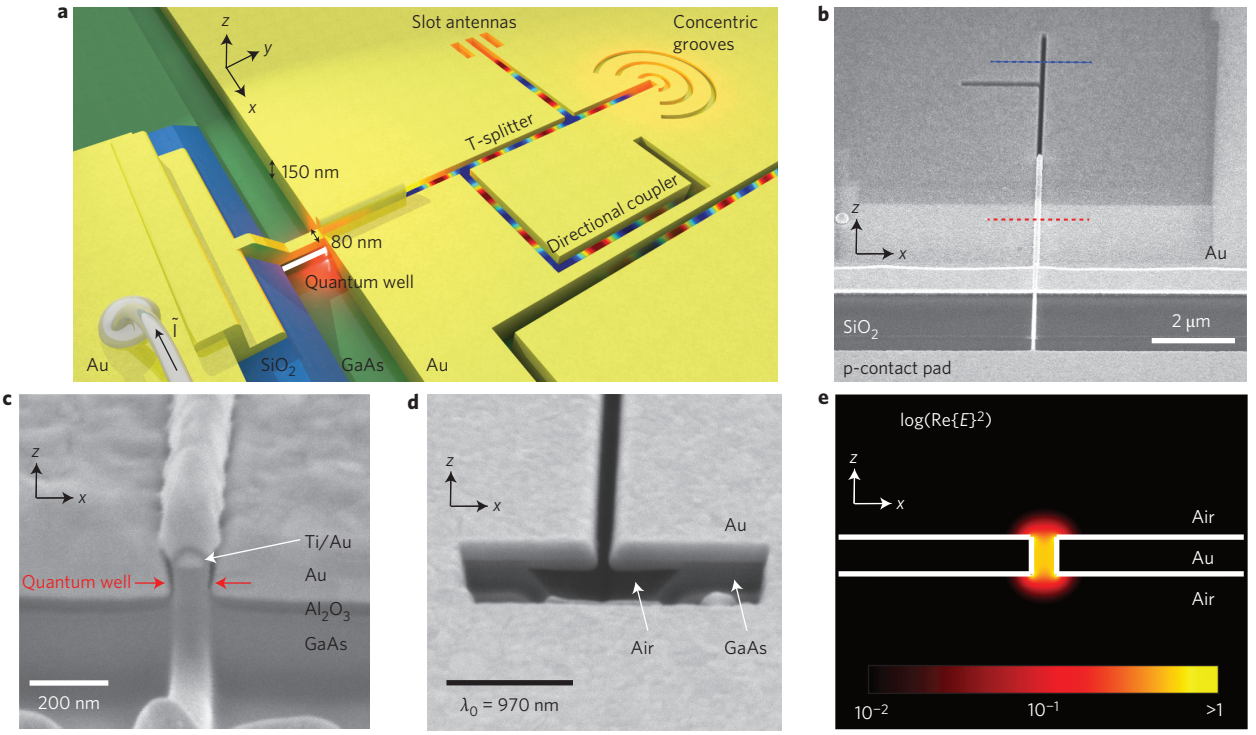

Figure 1 | Subwavelength slot-waveguide-coupled nano-LED platform. a, Schematic showing an integrated, electrically driven optical nanocircuit composed of three-dimensional slot-waveguide components, including two ultracompact splitters, a directional coupler and slot antennas. **b**, SEM image of a fabricated nano-LED coupled to a slot-waveguide-based T-splitter. Red and blue dashed lines indicate the position for the FIB milled cross-sections in **c** and **d**. **c**, The nano-LED, with the quantum well located between the two red arrows. **d**, A suspended slot waveguide generated by FIB milling and under-etching of the GaAs substrate. **e**, Mode profile of an 80-nm-wide and 150-nm-tall slot waveguide.

nano-LED. For devices built on a GaAs substrate, chemical wet etching is used to locally undercut the GaAs below the slot waveguide to avoid light leakage into the substrate (see Methods; Supplementary Figs 1–4, 8a,b). For devices built on oxidized AlGaAs substrates, vertical mode confinement is naturally provided by the low-index substrate (Supplementary Fig. 8c). Results obtained for devices on both types of substrate are compared and discussed in this Article. Under electrical current excitation, the nano-LED emission can be efficiently coupled into the subwavelength slot, which supports a gap plasmon due to spontaneous emission modification within the extremely small, metal-clad active region (Supplementary Figs 9–12). These plasmons can be routed through circuit elements such as those in Fig. 1a, including bends, T-splitters, free-space couplers and directional couplers.

A scanning electron microscope (SEM) image of a typical device built on a GaAs substrate is shown in Fig. 1b. Electrical current is delivered to the nano-LED via an electrode on a SiO_2 insulation pad. The p-contact eventually forms part of the metal cladding encasing the nano-LED, which aids the confinement of the light emission into a guided mode inside the ridge. As such, it performs simultaneous electrical and optical functions. The output facet ($+y$-direction) of the nano-LED is end-fire-coupled to the slot waveguide. For efficient excitation of the gap plasmon in the slot, a lateral alignment precision within a few tens of nanometres is required. Figure 1c is a tilted cross-sectional SEM image (through the red line in Fig. 1b) of a gold-coated quantum-well ridge. It shows a self-aligned Ti/Au p-electrode above the quantum well and the thin Al_2O_3 layer that insulates the n-GaAs substrate from the gold. Figure 1d presents a cross-section of the suspended gold slot waveguide (through the blue line in Fig. 1b). An air pocket can be observed under the 200-nm-thick gold slot as a result of the undercut. All deep subwavelength slot waveguides coupled to nano-LEDs presented in the rest of this Article have a cross-sectional area of $0.016\lambda_0^2$ (150 nm tall by 80 nm wide). Full-field electromagnetic simulations show that these waveguides support highly localized modes (Fig. 1e) with 55% of the guided power confined within the rectangular slot (Supplementary Figs 10–11, 13).

Performance of the gap plasmon source

Here we describe the optical properties of the source and the coupling of its emission into the slot waveguide. Figure 2a shows a top-view SEM image of a fabricated nano-LED featuring a 2.5-μm-long quantum-well ridge cavity on an oxidized AlGaAs substrate (Supplementary Figs 5–7, 8c). An image of the electroluminescence from this device is captured with an optical microscope and overlaid on the SEM image to analyse the spatial distribution of the emission. We see that all the emission emerges from the one end of the nano-LED not coated by gold, the spectral behaviour of which provides valuable information on the intrinsic optical properties of the source (without an attached waveguide), as discussed in detail later in this section. Figure 2b presents an SEM image and electroluminescence overlay for a nano-LED fabricated on a GaAs substrate fully integrated with an end-fire-coupled, 5-μm-long, 150-nm-thick and 80-nm-wide slot waveguide. Electroluminescence can be observed under standard operation conditions with 80 A cm^{-2} peak injection current in 10 ns pulses of 2.25 V junction bias. Scattering from the slot waveguide termination is clearly visible, demonstrating that the nano-LED source is injecting gap surface plasmon polaritons (SPPs) into the slot waveguide, which remain guided through the entire length of the slot. Further evidence for the gap plasmon propagation down the slot comes from polarization-dependent studies of the electroluminescence emission from the waveguide termination itself and from shallow gratings placed near the end of the waveguide (Supplementary Figs 14–17). Two-dimensionally confined MDM gap plasmons supported by these narrow slot waveguides are dominated by electric fields

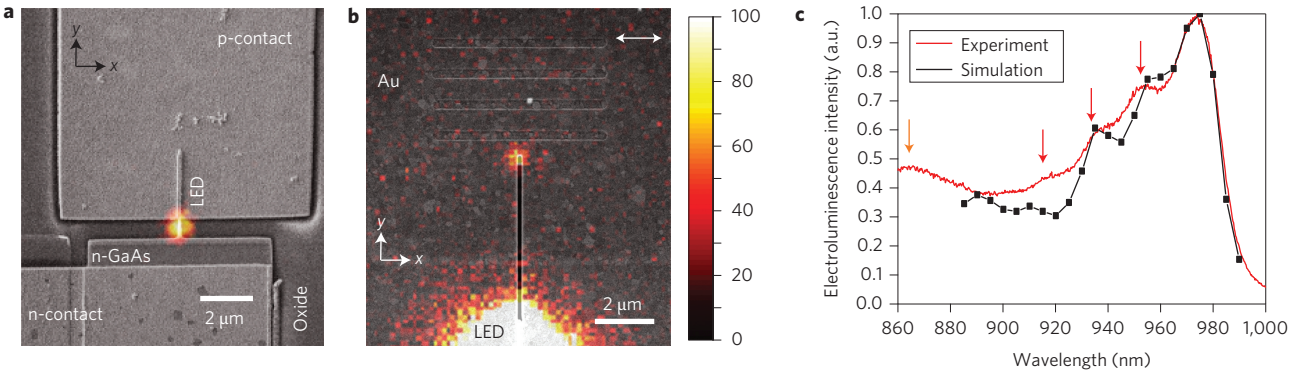

Figure 2 | Optical characterization of the nano-LED source. a, Electroluminescence emission map overlaid on an SEM image of a 2.5-μm-long nano-LED fabricated on an oxidized AlGaAs substrate. A single light output spot is observed in the gap between the p- and n-contacts. **b**, SEM image and electroluminescence image overlay of a nano-LED coupled to 5 μm slot waveguide. The collected electroluminescence with *x*-polarized detection shows a scattering spot at the end of the nano-LED-driven slot waveguide, consistent with the behaviour of gap plasmon guiding and outcoupling. **c**, Electroluminescence intensity spectrum collected from the device shown in **a** (red line) and the simulation predicted spectrum (black line). The red arrows indicate the positions of the Fabry-Pérot resonance wavelengths determined from the one-dimensional cavity model. The orange arrow indicates the emission from the GaAs barrier.

oriented normal to the direction of propagation[28–33]. As a result, the scattered light from the waveguide is *x*-polarized in this example. The undesired direct emission from the source region in this device is attributed to an insufficiently thick gold overlayer.

To gain further insight into the emission properties of the nano-LED, Fig. 2c presents the electroluminescence spectrum of the emission in Fig. 2a. The emission peak at 975 nm results from the InGaAs/GaAs quantum well. As the quantum well has a small conduction band offset of 80 meV, under high current injection a GaAs emission peak near 865 nm can also be observed due to carrier overflow into the barriers. The experimental spectrum exhibits clear Fabry–Pérot oscillations with a free spectral range of ~20 nm. Good agreement between the experimental and simulated spectra is found for every aspect, including the location of the resonances, the free spectral range and the amplitude of the Fabry–Perot resonances. The simulated spectrum was obtained by multiplying the measured electroluminescence spectrum from a large-area LED with the spatially averaged and wavelength-dependent Purcell factor obtained from full-field three-dimensional finite-difference time-domain simulations. To obtain this level of consistency without any fitting parameters, we had to account for the GaAs material dispersion, the gap plasmon mode dispersion and the gap plasmon reflection phase pickup at the terminations of the cavity, all of which are only dependent on known material optical properties[43] (Supplementary Figs 18–22 and Supplementary Methods). With the help of a simple Fabry–Pérot cavity model that assumes perfect reflections at the terminations of the nano-LED active region, one can use the spectral oscillation amplitude to estimate that the plasmon excitation efficiency inside the active region is at least 3.5%. A more refined full-field simulation-based estimate for the reflectivity of the cavity terminations[27] is 0.5, which results in a plasmon excitation efficiency of 14% inside the nano-LED (Supplementary Discussion).

The good agreement between the experimental and simulated electroluminescence spectra indicates that the source is emitting into a single gap plasmon cavity mode and provides good confidence in the use of simulations to estimate other performance parameters that are difficult to quantify experimentally with accuracy. Most notably, in the ideal structure where an 80-nm-wide quantum-well ridge is fully coated in gold on all sides and perfectly aligned to an output slot waveguide, guided plasmons in the slot can be excited with an efficiency of ~15–20% for the devices with oxidized AlGaAs substrates and ~5–10% for sources with GaAs substrates (Supplementary Fig. 12a). The estimated Purcell factor is 2, consistent with the observation of weak oscillations in the electroluminescence spectrum. With a Purcell factor of 2 combined with an intrinsic radiative lifetime of 1 ns in the InGaAs/GaAs quantum well, a 2 GHz modulation speed is readily achievable. By reducing the device width to 40 nm, the Purcell enhancement could reach a factor of 10 and allow for modulation at speeds in excess of 10 GHz (Supplementary Fig. 23). Further speed increases are accessible by reverse-biasing the LED during the turn-off cycle to shorten the minority carrier storage time (Supplementary Discussion).

Experimentally, the total system wall plug power efficiency for the electrically driven nanocircuit shown in Fig. 2b is 1.25×10^{-7} (detected scattered optical power from the end of the 5-μm-long waveguide divided by the input electrical power). This figure is calculated based on nano-LED dimensions of 80 nm × 4 μm, a 80 A cm^{-2} peak injection current in pulses of 10 ns duration at a repetition rate of 2 MHz and at 2.25 V, which produces 7,000 photons (1.28 eV) in the detector per second. As such, the drive power is $2.25\ \text{V} \times 80\ \text{A cm}^{-2} \times 10\ \text{ns bit}^{-1} \times 80\ \text{nm} \times 4\ \mu\text{m} \times 2.0 \times 10^{6}\ \text{Hz} = 1.15 \times 10^{7}\ \text{fJ s}^{-1}$. The outcoupled power arriving in the detector is $7{,}000\ \text{s}^{-1} \times 1.28\ \text{eV} \times 1.6 \times 10^{-19}\ \text{J eV}^{-1} = 1.43\ \text{fJ s}^{-1}$. The various factors contributing to the wall plug efficiency include the carrier injection efficiency, gap plasmon propagation loss, the radiation efficiency of the gap plasmon scattering from the end of the waveguide and the quantum-well internal quantum efficiency. From a more detailed analysis, it is clear that the major improvements of this device can come from the elimination of undesired current leakage and optical emission upward from the source region due to a gold overcoat of insufficient thickness (Supplementary Discussion).

Subwavelength optical nanocircuits

Our nano-LED platform facilitates the realization of several passive nanoscale slot-waveguide elements that have been proposed previously, but not yet verified experimentally. Such nanocircuit elements hold the promise of routing, splitting and manipulating optical signals at a length scale much smaller than the free-space diffraction limit[27–33,44]. A key element capable of both splitting surface plasmons and redirecting them in different directions is a T-junction. Figure 3a presents a bright-field microscope image of the nano-LED-coupled T-splitter. The lower gold slab is the wire-bonded electrical pad and the upper gold slab covering the quantum-well ridge can be patterned with routing elements, in

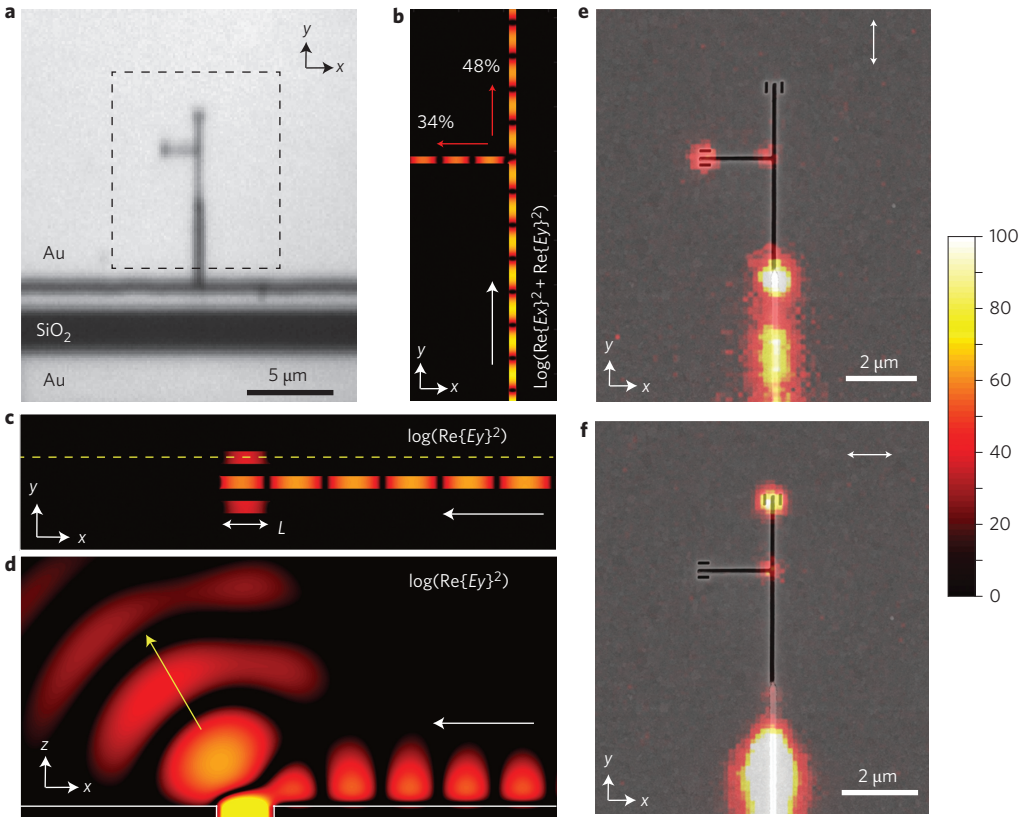

Figure 3 | Slot waveguide-based T-splitter and slot antennas. a, Optical image of a T-splitter-coupled nano-LED fabricated on a GaAs substrate. The black dashed rectangle outlines the region shown in **e** and **f**. **b**, Simulated electric field intensity for gap plasmon splitting at a T-junction. **c**, Top view of the simulated electric field intensity for a 320-nm-long, waveguide-fed slot antenna. **d**, Side view of the simulated electric field intensity for the waveguide-fed slot antenna across the yellow dashed line in **c**, showing free-space radiation. **e**, Electroluminescence scattering image with *y*-polarized detection overlaid on top of the SEM image of the device. **f**, Electroluminescence scattering image with *x*-polarized detection overlaid on top of the SEM image of the device.

this case a T-splitter. We performed full-field simulations for this geometry, which showed that 48% of the input gap plasmon is transmitted forward and 34% is split towards the left port (Fig. 3b). For this three-dimensional structure, some losses occur due to leakage into free space. We designed optical analogues to conventional slot antennas and placed them adjacent to the waveguide terminations to serve as free-space couplers for gap plasmons (Supplementary Fig. 24). The slot antennas are driven evanescently by the guided mode and support a half-wavelength standing-wave resonance for gap plasmons, which generate an equivalent magnetic dipole current parallel to the length of the slot. Figure 3c is a top view of the simulated *y*-polarized electric field intensity of two 320-nm-long, 80-nm-wide slot antennas, one on either side of the waveguide termination. The gap plasmon is launched from the right, propagates in the $-x$-direction and drives both slot antennas. An x–z plane display of the same simulation across the yellow dashed line in Fig. 3c is shown in Fig. 3d, which illustrates radiating fields polarized normal to the slot being emitted from the antenna. Simulations show that 40% of the input gap plasmons can be scattered to free space ($+z$ and $-z$ half space), which is 2.7 times greater than without the slot antennas, while reflections are reduced from 70% to 30% (Supplementary Fig. 24b).

SEM and electroluminescence image overlays of the area indicated by the black dashed rectangle in Fig. 3a are shown in Fig. 3e,f for the two orthogonal detection polarizations. For *y*-polarized detection (Fig. 3e), a scattering spot is observed at the T-junction as well as at the end of the slot waveguide transporting gap plasmons in the $-x$-direction. For *x*-polarized detection (Fig. 3f), a scattering spot also appears at the junction and a second spot is observed at the end of the waveguide propagating gap plasmons in the $+y$-direction. Both Fig. 3e and f exhibit consistent free-space coupling of the gap plasmon in the polarization normal to the direction of propagation. Not surprisingly, the T-junction partially decouples gap plasmons due to the presence of sharp corners and the finite aspect ratio (height:width = 150:80 nm) of the fabricated slots[27]. Although full-field simulations predict ~4% free-space leakage of the input gap plasmon at the junction (Supplementary Fig. 25), experimentally we observed that the junction scattering is comparable to the signal at the left port (predicted to outcouple ~14% of the input gap plasmon power upwards). The increased leakage may be attributed to the non-vertical sidewalls of the waveguide (with a larger slot width near the top gold surface; Fig. 1d). By comparing the integrated scattered light intensity from the two output ports, we find that the ratio of gap plasmon power coupled forward versus left is ~2:1, which is slightly higher than the theoretically calculated value of 1.4:1 (Fig. 3b). More equal splitting ratios can be obtained for waveguides with vertical sidewalls and higher aspect ratios (height versus width) that more closely resemble planar MDM slab waveguides (Supplementary Fig. 25b).

The highly reproducible fabrication process enabled us to build slot waveguide-based optical nanocircuits of greater complexity than straight waveguides, corners and splitters. Here, for the first time, we experimentally demonstrate a compact slot waveguide-based directional coupler with a coupling length of $\sim 2\lambda_0$. In comparison, typical dielectric waveguide-based directional couplers operate with coupling lengths in the range ~ 20–$100\lambda_0$ (refs 44–46). The extremely compact nature of our directional coupler is essential, as any practical waveguide-based circuit element must perform its function within an interaction length much shorter than the propagation decay length, which is ~ 5–$10\lambda_0$ depending on the

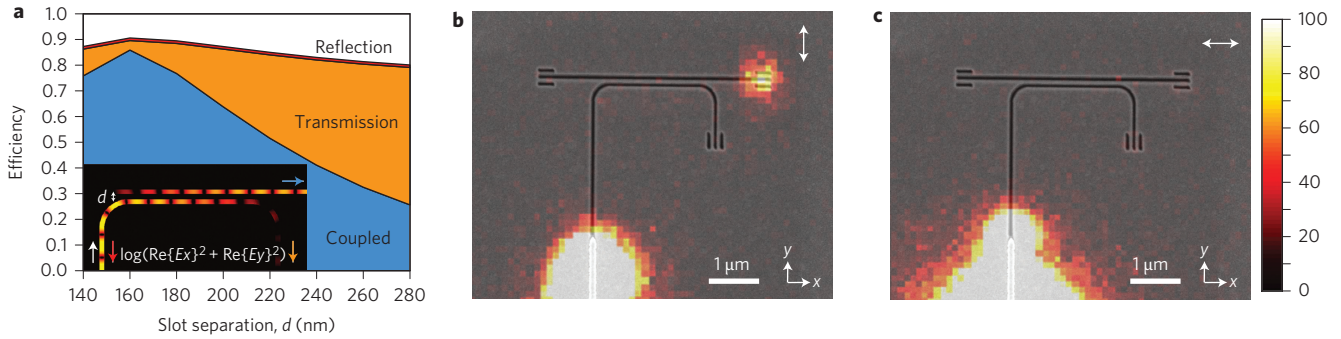

Figure 4 | Slot-waveguide-based directional coupler. a, Simulation of the coupling efficiency to each directional coupler output port as a function of the centre-to-centre separation d between two waveguides. Inset: simulated electric field intensity for a directional coupler with $d = 160$ nm. Gap plasmons are injected from the input port (white arrow), and can be reflected (red arrow), coupled (blue arrow) or transmitted (orange arrow). **b**, Electroluminescence scattering image with y-polarized detection overlaid on top of the device SEM image, showing emission from the coupled port. **c**, Electroluminescence scattering image with x-polarization sensitive detection overlaid on the device SEM image, showing no detectable scattering signal from the transmission port.

operating wavelength, slot aspect ratio and material[27,44]. To achieve complete power transfer, the two waveguides must have the same propagation wave vector. For simplicity, we chose the slots to have identical physical dimensions, both 150 nm high and 80 nm wide. They were milled and undercut simultaneously. Because the coupling length is inversely proportional to the coupling constant between the two slots given by $l_c = \pi/2\kappa$, where l_c is the coupling length and κ is the coupling constant[47], we would like to maximize κ by minimizing the separation between the waveguides. We chose a fixed $l_c = 2$ μm and performed full-field simulations to determine the separation for complete transfer. The inset to Fig. 4a shows a top view of the electric field profile of one such simulation where the input gap plasmon is excited from the bottom left port (white arrow), propagates through a 400-nm-radius curve, then couples to a nearby waveguide running in parallel separated by a centre-to-centre distance of $d = 160$ nm. The bottom-right port is the transmission port (orange arrow) and the top-right port is the coupled port (blue arrow). Figure 4a shows a simulation of the coupled efficiency, which is maximized at $d = 160$ nm (80-nm-thick gold separation wall). The fraction coupled is ~0.85 and the transmission is <0.05. There is ~0.01 reflection from the 400-nm-radius bend and 0.1 coupler loss. We compensated for the propagation loss of a single straight waveguide of the same length in the modelling to obtain the length-independent performance of the directional coupler. Figure 4b,c shows the SEM and electroluminescence image overlays of the completed device with y- and x-polarized detection, respectively. For y-polarized detection, only one scattering spot is observed at the coupled port apart from the direct radiation from the nano-LED. There is no radiation from the isolated port or the slot curves. For x-polarized detection, there is no observable scattering above the noise level, indicating that the transmitted power is negligible. If we conservatively assume the transmission is on the order of the noise level, the coupled versus transmitted power ratio is at least ~15 for gap plasmon directional coupling (>12 dB isolation).

Conclusions

In this Article, we have demonstrated the integration of nano-LEDs with deep-subwavelength plasmonic slot waveguides. The two-dimensionally confined modes of such waveguides enable flexible routing of optical signals and dense integration of complex nanophotonic circuit elements on a chip. To demonstrate this point, several basic electrically driven nanocircuits were realized. The emergence of light at the terminations of such circuits demonstrated that light can indeed be coupled into the waveguides and that the electrically generated plasmonic/optical signals can be manipulated in micrometre-scale circuits. The spectral properties of the light emission from the source also indicated the presence of a Purcell effect that can assist in the coupling of the LED emission into the single-mode slot waveguide. Although the wall-plug efficiency of the current nanocircuit is quite low, this work opens the door to the development of novel quantum plasmonic circuits, ultracompact sensing elements and ultracompact sources for optical communication that are capable of high-speed[36–41], single-mode emission[35,37]. Whereas nanolasers based on lossy metallic cavities require extremely high carrier densities and modal gain to achieve stimulated emission at room temperature[8–15,19,20], the slot-waveguide-coupled nano-LED platform allows for rapid extraction of surface plasmons out of the lossy metal region and into a low-loss single-mode waveguide[48,49]. Long-distance optical communication is dominated by the use of high-power lasers, but, as we continue to scale down optical cavities well below the wavelength of light for low-power, small-footprint operation in integrated on-chip systems, it becomes exponentially more difficult to achieve efficient stimulated emission. In this regime, the advantages of metal-clad single-mode nano-LEDs as an alternative on-chip light source become eminently clear.

Methods

Sample fabrication. The quantum well structure was grown by molecular beam epitaxy on an n-doped GaAs substrate, and consisted of a 300 nm n-doped GaAs layer, an 8 nm $In_{0.15}Ga_{0.85}As$ quantum well surrounded by 20 nm GaAs barriers and a 60 nm p-doped GaAs layer. The doping densities for the n-GaAs and p-GaAs were $2 \times 10^{18}cm^{-3}$ and $5 \times 10^{18}cm^{-3}$, respectively. A 200-nm-thick SiO_2 layer was deposited on the wafer by plasma-enhanced chemical vapour deposition then wet-etched with HF to transfer a photoresist pattern forming square insulation pads. Electron-beam-evaporated 15 nm Cr/200 nm Au square contact pads were defined on the SiO_2 by photoresist lift-off. Selective area plasma etching (BCl_3, Cl_2) of the wafer was used to expose the n-GaAs substrate, onto which Au/Ge/Ni/Au was evaporated and annealed at 450 °C to form the n-contact. A section of 60-nm-wide Ti/Au (2 nm/60 nm thick) p-electrode was defined and connected to the large contact pad by electron-beam lithography (EBL), 45° tilted electron-beam evaporation and lift-off. The sample was dipped into a 20:1 buffered oxide etch to remove the GaAs native oxide after EBL and before metal deposition. Using the p-electrode as a hard mask, a plasma etching step was performed to define the 130-nm-tall quantum well ridge, thus forming a self-aligned electrode on the nano-LED. A thin layer (5–10 nm) of Al_2O_3 was conformally deposited over the nano-LED and the substrate using atomic layer deposition to provide electrical insulation. To form the metal cladding and starting material for the slot waveguide, a thick layer of Au (150–200 nm) was deposited at a 45° angle in the $+y$-direction so that the output facet of the nano-LED was uncoated. Through careful alignment in the focused ion beam (FIB) tool, 80-nm-wide slots (and any other slot-based passive nanocircuit elements) were milled in the Au slab starting from the output facet of the nano-LED. Finally, the GaAs substrate directly beneath the slot elements was undercut by 400–500 nm using H_3PO_4:H_2O_2:H_2O (3:2:20) isotropic wet etching to complete the suspended MDM slot waveguide. Although optional, for the most reproducible nano-LED emission, the active quantum well ridge was enclosed and protected in a layer of resist during the wet etch using aligned EBL.

Full-field electromagnetic simulations. We performed full-field finite-difference time-domain simulations[50] using both in-house software and the publicly available code MEEP developed by MIT with a perfectly matched layer absorbing boundary condition to model the excitation and propagation of gap plasmons in the nano-LED and slot waveguide at 970 nm free-space wavelength. The spatial grid resolution was 5 nm. For electric field intensity distribution plots, the gap plasmons were excited in the slot waveguide using a single continuously oscillating electric dipole source placed at the centre of the slot oriented normal to the sidewalls. After the simulation had reached a steady state (typically 50 optical periods), the complex electric field at each spatial location was extracted and converted to intensity. For guided power calculations, the gap plasmons were excited in the slot waveguide using a single pulsed electric dipole source placed at the centre of the slot oriented normal to the sidewalls. We defined flux surfaces where the complex Poynting vector at the frequency of interest was calculated via a Fourier transform of the electric and magnetic field time transients.

Experimental set-up for optical measurements. Each device was wire-bonded and tested in an optical microscope set-up connected to a semiconductor parameter analyser. The sources were driven with a pulse generator outputting 10 ns pulses at 2 MHz with a voltage of 5–7 V and average current of 5–10 nA. The electroluminescence was imaged in the microscope set-up with a Pixis 1024 thermoelectrically cooled Si charge-coupled device after collection with a $\times 100$, NA = 0.9 objective and transmission through a rotatable polarizer. The average current was measured concurrently using a Keithley picoammeter. For 4-μm-long devices, the typical operating range of the current density was between 1 and 10 A cm^{-2}.

Received 9 October 2013; accepted 28 December 2013; published online 23 February 2014

References

1. Gramotnev, D. K. & Bozhevolnyi S. Plasmonics beyond the diffraction limit. *Nature Photon.* **4,** 83–91 (2010).
2. Papaioannou, S. *et al.* A 320 Gb/s throughput 2 × 2 silicon-plasmonic router architecture for optical interconnects. *J. Lightwave Technol.* **29,** 3185–3195 (2011)
3. De Leon, N. P., Lukin, M. D. & Park, H. Quantum plasmonic circuits. *IEEE J. Quantum Electron.* **18,** 1781–1791 (2012).
4. Anker, J. N. *et al.* Biosensing with plasmonic nanosensors. *Nature Mater.* **7,** 442–453 (2008).
5. Service, R. F. Ever-smaller lasers pave the way for data highways made of light. *Science* **328,** 810–811 (2010).
6. Noda, S. Seeking the ultimate nanolaser. *Science* **314,** 260–261 (2006).
7. Khajavikhan, M. *et al.* Thresholdless nanoscale coaxial lasers. *Nature* **482,** 204–207 (2012).
8. Hill, M. T. *et al.* Lasing in metallic-coated nanocavities. *Nature Photon.* **1,** 589–594 (2007).
9. Marell, M. J. H. *et al.* Plasmonic distributed feedback lasers at telecommunications wavelengths. *Opt. Express* **19,** 15109–15118 (2011).
10. Kwon, S.-H. *et al.* Subwavelength plasmonic lasing from a semiconductor nanodisk with silver nanopan cavity. *Nano Lett.* **10,** 3679–3683 (2010).
11. Noginov, M. A. *et al.* Demonstration of a spaser-based nanolaser. *Nature* **460,** 1110–1112 (2009).
12. Oulton, R. F. *et al.* Plasmon lasers at deep subwavelength scale. *Nature* **461,** 629–632 (2009).
13. Yu, K., Lakhani, A. & Wu, M. C. Subwavelength metal-optic semiconductor nanopatch lasers. *Opt. Express* **18,** 8790–8799 (2010).
14. Nezhad, M. P. *et al.* Room-temperature subwavelength metallo-dielectric lasers. *Nature Photon.* **4,** 395–399 (2010).
15. Chen, R. *et al.* Nanolasers grown on silicon. *Nature Photon.* **5,** 170–175 (2011).
16. Ellis, B. *et al.* Ultralow-threshold electrically pumped quantum-dot photonic-crystal nanocavity laser. *Nature Photon.* **5,** 297–300 (2011).
17. Loncar, M., Yoshie, T., Scherer, A., Gogna, P. & Qiu, Y. Low-threshold photonic crystal laser. *Appl. Phys. Lett.* **81,** 2680–2682 (2002).
18. Noda, S. Photonic crystal lasers—ultimate nanolasers and broad-area coherent lasers. *J. Opt. Soc. Am. B* **27,** B1–B8 (2010).
19. Khurgin, J. B. & Sun, G. Injection pumped single mode surface plasmon injection pumped single mode surface plasmon generators: threshold, linewidth, and coherence. *Opt. Express* **20,** 15309–15325 (2012).
20. Khurgin, J. B. & Sun, G. How small can 'Nano' be in a 'Nanolaser'? *Nanophotonics* **1,** 3–8 (2012).
21. Okamoto, K. *et al.* Surface-plasmon-enhanced light emitters based on InGaN quantum wells. *Nature Mater.* **3,** 601–605 (2004).
22. Koller, D. M. *et al.* Organic plasmon-emitting diode. *Nature Photon.* **2,** 684–687 (2008).
23. Walters, R. J., van Loon, R. V. A., Brunets, I., Schmitz, J. & Polman, A. A silicon-based electrical source of surface plasmon polaritons. *Nature Mater.* **9,** 21–25 (2010).
24. Neutens, P., Lagae, L., Borghs, G. & Van Dorpe, P. Electrical excitation of confined surface plasmon polaritons in metallic slot waveguides. *Nano Lett.* **10,** 1429–1432 (2010).
25. Veronis, G. & Fan, S. Theoretical investigation of compact couplers between dielectric slab waveguides and two-dimensional metal–dielectric–metal plasmonic waveguides. *Opt. Express* **15,** 1211–1221 (2007).
26. Brongersma, M. L. *et al.* in *Plasmonic Nanoguides and Circuits* (ed. Bozhevolnyi, S.) Ch. 13 (Pan Stanford, 2008).
27. Cai, W., Shin, W., Fan, S. & Brongersma, M. L. Elements for plasmonic nanocircuits with three-dimensional slot waveguides. *Adv. Mater.* **22,** 5120–5124 (2010).
28. Veronis, G. & Fan, S. Modes of subwavelength plasmonic slot waveguides. *J. Lightwave Technol.* **25,** 2511–2521 (2007).
29. Kurokawa, Y. & Miyazaki, H. T. Metal–insulator–metal plasmon nanocavities: analysis of optical properties. *Phys. Rev. B* **75,** 035411 (2007).
30. Pile, D. F. P. & Gramotnev, D. Plasmonic subwavelength waveguides: next to zero losses at sharp bends. *Opt. Lett.* **30,** 1186–1188 (2005).
31. Pile, D. F. P. *et al.* Two-dimensionally localized modes of a nanoscale gap plasmon waveguide. *Appl. Phys. Lett.* **87,** 261114 (2005).
32. Pile, D. F. P., Gramotnev, G. K., Rupert, O. F. & Zhang, X. On long-range plasmonic modes in metallic gaps. *Opt. Express* **15,** 13669–13674 (2007).
33. Pile, D. F. P. & Gramotnev, G. K. Channel plasmon–polariton in a triangular groove on a metal surface. *Opt. Lett.* **29,** 1069–1071 (2004).
34. Jun, Y. C., Kekatpure, R. D., White, J. S. & Brongersma, M. L. Nonresonant enhancement of spontaneous emission in metal–dielectric–metal plasmon waveguide structures. *Phys. Rev. B* **78,** 153111 (2008).
35. Jun, Y. C., Huang, K. C. Y. & Brongersma, M. L. Plasmonic beaming and active control over fluorescent emission. *Nature Commun.* **2,** 283 (2011).
36. Lau, E. K., Lakhani, A., Tucker, R. S. & Wu, M. C. Enhanced modulation bandwidth of nanocavity light emitting devices. *Opt. Express* **17,** 7790–7799 (2009).
37. Shambat, G. *et al.* Ultrafast direct modulation of a single-mode photonic crystal nanocavity light-emitting diode. *Nature Commun.* **2,** 539 (2011).
38. Suhr, T., Gregersen, N., Yvind, K. & Mork, J. Modulation response of nanoLEDs and nanolasers exploiting Purcell enhanced spontaneous emission. *Opt. Express* **18,** 11230–11241 (2010).
39. Chen, C. *et al.* GHz bandwidth GaAs light-emitting diodes. *Appl. Phys. Lett.* **74,** 3140–3142 (1999).
40. Fattal, D. *et al.* Design of an efficient light-emitting diode with 10 GHz modulation bandwidth. *Appl. Phys. Lett.* **93,** 243501 (2008).
41. Walter, G., Wu, C. H., Then, H. W., Feng, M. & Holonyak, N. Jr. Tilted-charge high speed (7 GHz) light emitting diode. *Appl. Phys. Lett.* **94,** 231125 (2009).
42. Miller, D. A. B. Device requirements for optical interconnects to silicon chips. *Proc. IEEE* **97,** 1166–1185 (2009).
43. Palik, E. D. *Handbook of Optical Constants of Solids* (Academic, 1985).
44. Bozhevolnyi, S., Volkov, V., Devaux, E., Laluet, J. & Ebbesen, T. Channel plasmon sub-wavelength waveguide components including interferometers and ring resonators. *Nature* **440,** 508–511 (2006).
45. Zablocki, M. J., Sharkawy, A., Ebil, O., Shi, S. & Prather, D. Electro-optically switched compact coupled photonic crystal waveguide directional coupler. *Appl. Phys. Lett.* **96,** 081110 (2010).
46. Zenin, V. A. *et al.* Directional coupling in channel plasmon–polariton waveguides. *Opt. Express* **20,** 6124–6134 (2012).
47. Haus, H. A. *Waves and Fields in Optoelectronics* (Prentice-Hall, 1984).
48. Chen, L., Shakya, J. & Lipson, M. Subwavelength confinement in an integrated metal slot waveguide on silicon. *Opt. Lett.* **31,** 2133–2135 (2006).
49. Hryciw, A., Jun. Y. C. & Brongersma, M. L. Electrifying plasmonics on silicon. *Nature Mater.* **9,** 3–4 (2010).
50. Taflove, A. & Hagness, S. C. *Computational Electrodynamics: The Finite-Difference Time-Domain Method* 3rd edn (Artech House, 2005).

Acknowledgements

The authors acknowledge funding support from the Air Force Office of Scientific Research (G. Pomrenke, grant no. FA9550-10-1-0264). M.-K.S. acknowledges support for this work by the Basic Science Research Program (2011-0015119 and 2009-0087691) of National Research Foundation of Korea and the Korean Ministry of Education. The authors thank W. Cai and A. Curto for discussions.

Author contributions

M.-K.S. and M.L.B. conceived the idea. K.C.Y.H. and M.-K.S. designed the structures. Y.H. and T.S. performed the molecular beam epitaxial growth of the quantum-well structure under the supervision of J.S.H. K.C.Y.H. and M.-K.S. performed theoretical calculations and full-field simulations. K.C.Y.H. and M.-K.S. fabricated and characterized the samples. K.C.Y.H. and M.L.B. wrote the manuscript. M.L.B. supervised the project.

Additional information

Supplementary information is available in the online version of the paper. Reprints and permissions information is available online at www.nature.com/reprints. Correspondence and requests for materials should be addressed to M.K.S. and M.L.B.

Competing financial interests

The authors declare no competing financial interests.